Hindawi
Journal of Nanomaterials
Volume 2017, Article ID 9095301, 11 pages
https://doi.org/10.1155/2017/9095301

Research Article

Influence of Carbon Modification on the Morphological, Structural, and Optical Properties of Zinc Oxide Nanoparticles Synthesized by Pneumatic Spray Pyrolysis Technique

R. Taziwa,[1,2] E. Meyer,[1] D. Katwire,[2] and L. Ntozakhe[1,2]

[1]*Fort Hare Institute of Technology (FHIT), University of Fort Hare, Private Bag X1314, Alice 5700, South Africa*
[2]*Chemistry Department, University of Fort Hare, Private Bag X1314, Alice 5700, South Africa*

Correspondence should be addressed to R. Taziwa; rtaziwa@ufh.ac.za

Received 25 March 2017; Accepted 11 July 2017; Published 6 September 2017

Academic Editor: Meng Zhang

This paper reveals the influence of doping on the morphological, structural, and optical properties of zinc oxide (ZnO) nanoparticles (NPs) synthesized by pneumatic spray pyrolysis technique (PSP), using zinc ethoxide $Zn(O_2CH_3)_2$ as the precursor. The prepared samples were characterized by XRD, HRTEM, SEM-EDX, UV-Vis spectroscopy, and RS. RS analysis has revealed that the unmodified ZnO and carbon modified ZnO samples have characteristic Raman optic modes at 325 cm^{-1}, 373 cm^{-1}, and 432 cm^{-1} belonging to Wurtzite ZnO structure. The XRD ZnO (C:ZnO) NPS have characteristic peaks of hexagonal Wurtzite ZnO structure. HRTEM analysis has revealed that the synthesized ZnO NPs have particle size range of 8.8–11.82 nm. EDX spectra of both unmodified and modified ZnO nanoparticles have revealed prominent peaks at 0.51 keV, 1.01 keV, 1.49 keV, 8.87 keV, and 9.86 keV. The occurrence of these peaks in the EDX spectra endorses the existence of Zn and O atoms in the PSP synthesized ZnO NPs. The UV-Vis spectroscopy has revealed a red shift of the absorption edge, with the increase in C dopant level. The effect of nanocrystallite size and the gradual prominence of C into ZnO matrix due to increase in C dopant level in the PSP synthesized ZnO NPs was meticulously elaborated through Raman spectroscopy analysis.

1. Introduction

The development of semiconductor metal oxides has become an area of significant research interest because it is considered as a potential approach to solve energy issues [1]. More particularly, ZnO metal oxide semiconductor nanoparticles (NPs) have received significant attention due to their enhanced technological applications, mainly because of the rare properties observed at nanoscale [2–4]. Nanosized ZnO NPs have been intensively studied due of their extraordinary large exciton binding energy of 60 meV, extraordinary photosensitivity, nontoxic nature, wide bandgap, and the fact that they present low cost materials for fabrication of solar cell electrodes [3–5]. Moreover, the morphologies of ZnO nanomaterials can be easily modified and controlled by a chemical reaction, which is an important factor influencing the performance of these nanomaterials for many technological applications [5–7]. It has been reported that modification of ZnO has an effect on the structural, electronic, and optical properties [8]. Lately, efforts have been dedicated to the fabrication of modified ZnO nanocrystallites in order to enhance the structural, morphological, and optical properties of materials by modification of the surface properties, such as crystal deficiencies, electronic band gap, specific surface area, and O vacancies. Doping with nonmetallic elements such as carbon, nitrogen, and sulphur has also been considered to reduce the bandgap of ZnO semiconductors [8–10]. Specifically, carbon atoms have been usually employed as the dopant to change the morphological, structural, optical, and electronic properties of nano-ZnO because of the almost equivalent size with oxygen atoms. Moreover, the substitutional doping of atoms of similar size requires low energy and, hence, it occurs rather easily as compared to substitutional doping of atoms of different atomic radii. Hence, the replacement of O (oxygen)

atom by C carbon atoms in the ZnO matrix has favourable thermodynamics compared to other nonmetal dopants. However, to date, the use of C-modified ZnO nanomaterials has been modest because of the scarcity of scientific articles that report on the effect of change of nanomaterial properties due to introduction of dopants. It has been theorized that the introduction of dopants improves both the optical and structural properties of ZnO. Therefore, to realize the full potential of ZnO nanomaterials for applications as electrode materials for solar cell devices, it is vital to investigate change in nanomaterials properties due to nonmetal doping.

Numerous techniques have been employed to fabricate unmodified and modified ZnO NPs, including solid state techniques, spray pyrolysis technique, microwave heating process, hydrothermal techniques, chemical coprecipitation method, chemical vapour deposition (CVD), and sol-gel techniques [3, 10–18]. The morphology, crystalline structure, and mole ratio (stoichiometry) of ZnO thin films are dependable on the deposition conditions [11]. These variations arise from insignificant changes in the deposition parameters and conditions. The inherent necessity for stoichiometric ZnO films suggests that a deposition method where the film stoichiometry is controlled by a chemical reaction would enable more consistent results. Moreover, it is an inherent requirement, when developing new methods for deposition of electrodes for low cost solar cells, to keep the deposition system as simple as possible, maximize throughput, and keep costs at a minimum. Spray pyrolysis (SP) methods offer such an opportunity.

SP methods offer the opportunity to precisely control the structural, optical, and electronic properties of nanomaterials, since the stoichiometry of the chemical precursors is governed by chemical reactions [19, 20]. Moreover, aerosol processes have the potential to replace primordial costly and problematical solid state techniques for fabrication of ZnO nanostructures like the derivatives of chemical vapour deposition techniques such as plasma enhanced chemical vapour deposition (PECVD) [12–18] and to eliminate costly and sophisticated solid state techniques like evaporation plasma [21], anodization [22, 23], spin on methods [24–26], sputtering [15], ion assisted deposition [27], reactive ion plating [28], laser ablation [29], filtered arc deposition [30], and atomic layer epitaxy [31]. These techniques have numerous disadvantages that limit their application on industrial scale, such as high vacuum pressure chambers requirements and high thermal processing budgets, which increase the cost of production of ZnO nanostructures and in turn increase the overall cost of production of solar cell devices with ZnO nanostructures. Moreover, the SP systems have operational simplicity; nanoparticles produced have consistent structural, optical, and electronic properties. Also nanoparticles are produced in a one-step process without need for further purification or excessive drying procedures, which has an impact on the total thermal budget and cost of production of ZnO nanostructures. Likewise, the technique can be used to coat large substrates and presents the opportunity for industrial scaling. It shows a very simple and relatively cost effective method, unlike many other film deposition techniques. The present study exposes novel morphological, structural, and optical properties of carbon modified ZnO NPs prepared by pneumatic spray pyrolysis (PSP) technique. Furthermore, the dearth of specific research articles that report on the influence of carbon modification on nanomaterial properties of ZnO deposited by economical spray pyrolysis techniques was also the main stimulus of the current compilation.

Table 1: Preparation of precursor of unmodified and C:ZnO precursors' solutions.

Sample #	Mass of $Zn(O_2CH_3)_2$ (g)	Volume of TBA (ml)
Unmodified	5.4923	0
0.005_{TBA}C-ZnO	5.4925	0.78
0.01_{TBA}C-ZnO	5.4921	1.55
0.015_{TBA}C-ZnO	5.4924	2.33

2. Experimental

2.1. Synthesis of Unmodified Zinc Oxide and Modified Zinc Oxide Nanoparticles. The mechanism for the production of C:ZnO NPs is comparable to the one employed by Taziwa et al. [32, 33] in the fabrication of carbon modified titanium dioxide NPs, which is as follows:

$$\begin{aligned} &Zn(O_2CCH_3)_{2(s)} + 4CH_3CH_2OH_{(aq)} \\ &\quad \longrightarrow Zn(OCH_2CH_3)_{4(aq)} + CH_3CO_2H_{(aq)} \\ &Zn(OCH_2CH_3)_{4(aq)} + CH_3CO_2H_{(aq)} \\ &\quad \xrightarrow{\text{TBA+Pyrolysis@400}^\circ\text{C}} ZnO_{2-x}C_{x(s)} + CO_{2(g)} + H_2O_{(g)}. \end{aligned} \tag{1}$$

In typical synthesis procedure, 0.1 M of zinc acetate solution was prepared by adding 5.4923 g $Zn(O_2CH_3)_2$ to a 250 ml volumetric flask, containing a minimum amount of ethanol (99.99%) sigma Aldrich, resulting in the formation of zinc ethoxide, as depicted by (1). A minimum amount of acetic acid (CH_3COOH) was transferred to volumetric flask containing zinc ethoxide. The zinc ethoxide solution was sonicated on an ultrasonicator at 40°C for 30 minutes. 7.81 ml of tetrabutylammonium bromide (TBA) ($C_{16}H_{36}BrN$) was added to the resulting colourless solution of $Zn(O_2CH_3)_2$ in a 250 ml volumetric flask. The volumetric flask containing $Zn(O_2CH_3)_2$ and ($C_{16}H_{36}BrN$) was topped up to the mark with absolute ethanol. Additional precursor solutions containing different levels of the carbon dopant ($C_{16}H_{36}BrN$) were synthesized in much the same way. The only difference was the volume of the dopant solution, as shown here in Table 1.

The ZnO precursor ($Zn(O_2CH_3)_2$ + ($C_{16}H_{36}BrN$) + C_2H_6O) solution was then transferred into a chamber connected to a pneumatic pump prior to spray deposition. PSP deposition of unmodified and carbon modified ZnO nanoparticles was done on glass substrate at a deposition temperature of 400°C.

2.2. Spray Deposition. PSP technique involves forcing the precursor liquid through fine nozzles to produce smog of the

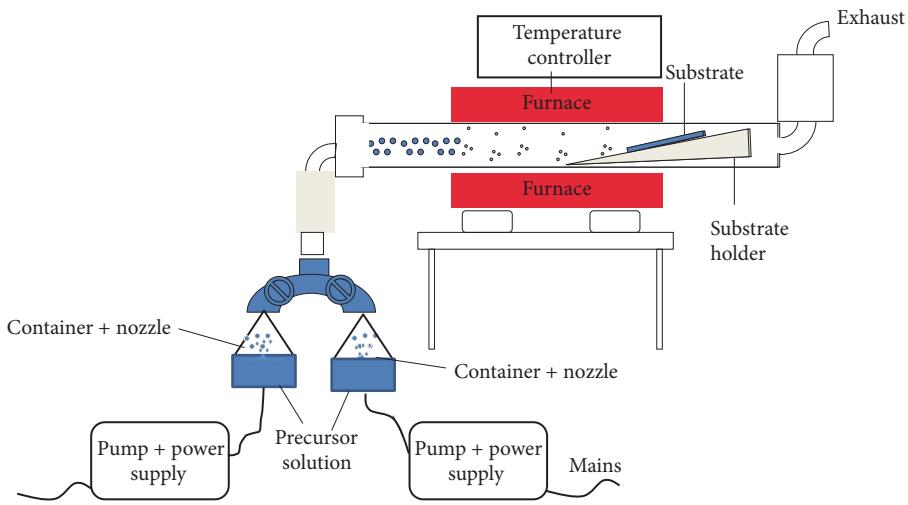

Figure 1: A graphic presentation of PSP system employed in the fabrication of unmodified and carbon modified ZnO NPs.

precursor liquid at audible sound. The precursor droplets are then generated in a chamber that was housing the pneumatic nebulizer transported to a heated zone through a PSP reaction chamber, such as glass or aluminium tubing, onto a preheated substrate. Pneumatic spray deposition was carried out for 4 hours to achieve the desired thin film thickness of less than 10 μm. Figure 1 shows a schematic representation of the actual experimental set used in production of unmodified and modified zinc oxide NPs reprinted with permission [32].

2.3. Characterizations. To evaluate the morphological, structural, and optical electronic properties of unmodified ZnO and C:ZnO NPs (0.005M_{TBA}C-ZnO_2, 0.01M_{TBA}C-ZnO_2, and 0.015M_{TBA}C-ZnO_2), various instrumental techniques were employed. To obtain the crystallographic phase and associated parameters of ZnO samples of the synthesized NPs, XRD spectra were obtained, using a Bruker D8 Advance X-ray diffractometer (XRD) with a Cu anode, generating K_α radiation of wavelength 1.544 Å and operating at 40 kV and 40 mA. XRD θ–2θ patterns of ZnO nanopowders synthesized by PSP were recorded in the 2θ range of 30°–100° at room temperature. Field Emission Scanning Electron Microscope (FE-SEM) Zeiss Auriga SEM equipped with EDS with Smart SEM software was used to study the elemental, structural, and morphological properties of ZnO nanostructures at an accelerating voltage of 30 KV. In order to determine the finer details relating to structural properties of unmodified and carbon modified ZnO, samples prepared by PSP technique were obtained using a JEOL JEM 2100 High Resolution Transmission Electron Microscope operating at 200 KV for high resolution images with selected area electron diffraction (SAED) patterns. Raman spectra of the ZnO samples were done using a Confocal Raman Imaging system (WITec GmbH, Ulm, Germany) alpha300RS. A fiber coupled DPSS laser 532 nm with a maximum output power after a single-mode fiber coupling of 44 mW was used as the excitation source. Data was then collected, using a multimode fiber into a high throughput lens based spectrograph (UHTS 300) with 300 mm focal length and two gratings 600 g/mm and 1800 g/mm, both blazed at 550 nm. The UHTS 300 spectrograph is connected with a Peltier cooled back illuminated CCD camera with better than 90% QE in the visible excitation. Each spectrum was acquired at an integration time of 1.09667 s and about 200 accumulations were collected per each spectrum in the scan range 100–1100 cm^{-1}.

3. Results and Discussions

3.1. XRD Analysis. Nanoparticulate size may be determined by using the peak broadening of the peaks in the XRD pattern. In this work, we have employed the Scherrer method [26], which is considered as a standard method. The Scherrer equation is depicted here in the equation:

$$\tau = \frac{K\lambda}{\beta \cos\theta}, \tag{2}$$

where τ is the mean nanoparticle size, which is a volume average, K is a shape factor, λ is the wavelength of the X-rays, β is the full width at half maximum in radians, and θ is the angle between the X-ray source and the detector. The value of K depends on the shape of the particles and here the value 0.9, which is a customary value for spherical NPs, has been used.

XRD $\theta - 2\theta$ patterns of ZnO nanopowders synthesized by PSP technique were recorded in the 2θ range of 30–80° at 25°C and depicted here in Figure 2. The XRD patterns of unmodified ZnO NPs exhibited the characteristic peaks of hexagonal Wurtzite structure. In fact, in all the diffractograms obtained at room temperature, XRD lines were observed at 31.90°, 34.50°, 36.34°, 47.73°, 56.88°, 63.04°, 68.20°, and 77.33°. These lines are indexed as (100), (002), (101), (102), (110), (103), (200), and (112), respectively. The presence of these peaks in the carbon modified zinc oxide (C-ZnO) samples confirms that the as-synthesized C-ZnO nanopowders have a hexagonal Wurtzite structure. Moreover, the XRD diffractograms have revealed sharp and intense peaks for the dominant peak

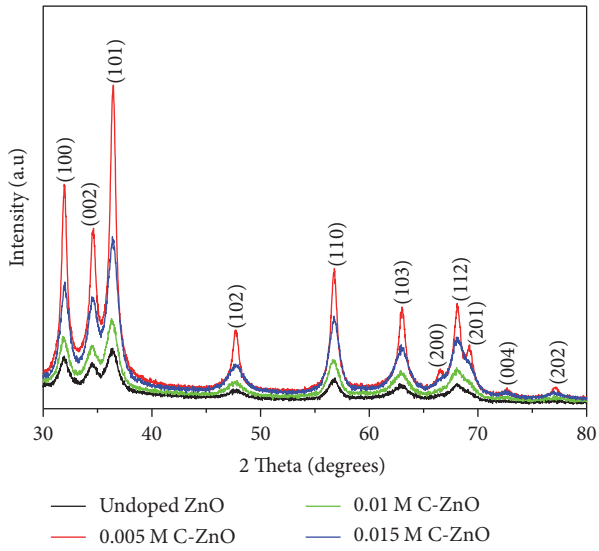

FIGURE 2: XRD patterns of ZnO nanoparticle deposited by a PSP technique.

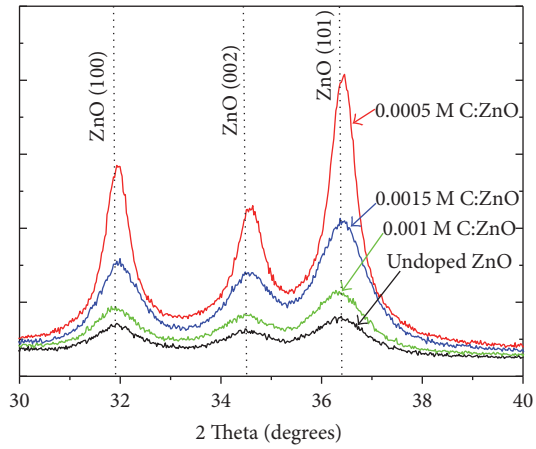

FIGURE 3: XRD peaks positions for the (100), (002), and (001) planes as a function of C dopant level of the PSP fabricated ZnO.

at 36.34° indexed (101), which reveals that the samples are highly crystalline. In addition, the XRD diffractograms of the C-ZnO NPs have revealed additional peaks that are indexed as (004) and (202), which were due to the incorporation of carbon in the ZnO matrix. Moreover, the 0.005 M C:ZnO sample has also revealed the existence of the peaks indexed (200) and (201), which are possible due to other impurities in the sample.

It is well acknowledged that the lattice distortion, due to defects, may cause a shift in the XRD peaks positions, depending on the type of strain in the crystal structure. Tensile or compressive strain causes the XRD peak positions to shift to either higher or lower angle [34]. Since the atomic radius of C $r = 0.77$ Å is bigger than that of O $r = 0.65$ Å, C substitution in ZnO lattice results in tensile strain along with the increase of crystallite size. This observation is in agreement with the calculated crystallite size from (2), which reveals an increase in ZnO NPs size with corresponding increase in the amount of C dopant level, as illustrated here in Table 2. This is a clear indication of the incorporation of C into ZnO lattice. Thus, we can conclude that, similarly, like previous reports on N doping [34, 35], C doping into ZnO lattice can be observed through peak broadening and shift of the most prominent peak (101) of the XRD diffractograms of ZnO, since peak broadening reflects an alteration of crystallite size.

The incorporation of C atoms into ZnO lattice and the influence of C doping on the ZnO crystal structure have been cross-examined by monitoring the three dominate peaks positions of the (100), (002), and (001) planes as illustrated here in Figure 3. Previous studies on the incorporation of Ag species [36] N [35] in ZnO lattice and C in TiO_2 [8] lattice have revealed that interstitial doping results in peak shift to lower 2θ values, whereas substitutional doping of either N or C in ZnO lattice results in peaks shifts to higher 2θ values [1, 8, 34, 35]. The three main peak positions of C:ZnO NPs shown in (Figure 3) reveal that carbon doping results in a peak shift to higher 2θ values, which indicates substitutional doping in ZnO samples. This confirms the results from the calculated crystallite size of the dominant diffraction plane (101), which indicates an increase in crystallite size, with an increase in carbon doping.

3.2. SEM Analysis. Figure 4 Shows the typical SEM micrographs of the unmodified and C-ZnO NPs synthesized by PSP technique with levels of carbon doping. The SEM images, both unmodified and C-ZnO samples, reveal the formation of spherical shaped ZnO NPs. The SEM micrographs reveal that the morphology and shape of both unmodified and C-ZnO change as the dopant level increases. Figure 4(a) exhibits the SEM image of the unmodified ZnO NPs, consisting of a mesoporous nanostructure with small spherical nanoparticles (4-5) around a central nanoparticle. In addition, the SEM micrographs of unmodified ZnO NPs clearly reveal well-defined individual smooth small nanoparticles that are easily distinguishable from each other. Figure 4(b) presents the SEM micrograph of 0.005 M C-ZnO NPs revealing similar nanostructure arrangement as with the unmodified ZnO sample. However, the introduction of carbon into the ZnO nanostructure results in the formation of larger agglomerates. The central atom in C-ZnO NPs is larger, as compared to the unmodified ZnO sample. Moreover, there is an increase in agglomeration as evidenced by the larger number of nanoclusters with larger central nanoparticle, as compared to the unmodified ZnO sample. This is in line with the XRD analysis which showed an increase in calculated nanoparticle size with carbon doping. XRD analysis revealed that the calculated NPs size for unmodified ZnO was between 11.30 and 12.50 nm and increased to 16.28–17.38 nm with carbon doping. In addition, on close inspection of the three dominate peaks pattern for the unmodified and 0.005 C-ZnO samples, evidence revealed that carbon doping resulted in peaks shifts to higher 2θ, which further endorses an increase in particle size coupled with an increase in carbon dopant level. This

Table 2: The position of the main diffraction peaks and average crystallite size calculated from XRD patterns of the fabricated ZnO NPs.

Sample #	ZnO(100) peak position (°)	ZnO(002) peak position (°)	ZnO(101) peak position (°)	XRD crystallite size (nm) (100)	XRD crystallite size (nm) (002)	XRD crystallite size (nm) (101)
Unmodified	31.97	34.35	36.22	11.30	12.50	9.60
0.005_{TBA}C-ZnO	31.97	34.35	36.22	16.56	17.38	16.28
0.01_{TBA}C-ZnO	31.97	34.35	36.22	10.69	13.68	9.99
0.015_{TBA}C-ZnO	31.97	34.35	36.22	10.70	12.40	9.96

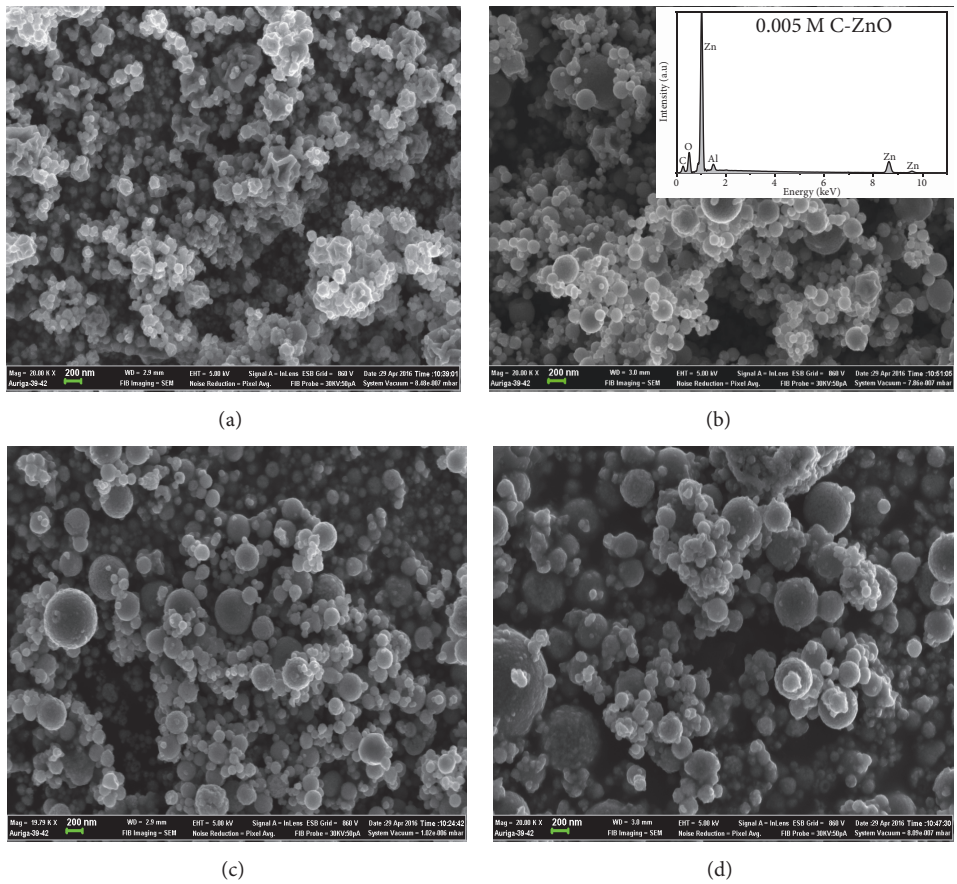

Figure 4: SEM micrographs of (a) unmodified ZnO, (b) 0.005 M C-ZnO, (c) 0.01 M C:ZnO, and (d) 0.015 M C:ZnO samples. Additionally, insert in (b) shows typical EDX spectra of 0.005 M C-ZnO nanostructures, respectively.

observation is in close agreement with the SEM images analysis shown here in (Figure 4).

Figures 4(c) and 4(d) show SEM micrographs of the (c) 0.01 C-ZnO samples and (d) 0.015 M C-ZnO samples with increasing dopant levels. The SEM micrographs clearly reveal the formation of agglomerates consisting of 4-5 small smooth spherical nanoparticles around a much larger central nanoparticle, as compared to the SEM micrographs shown in Figures 4(a) and 4(b). From the SEM images, it can be seen that increasing carbon concentration up to above 0.01 M resulted in increased agglomeration of NPs. This is due to the kinetic equilibrium process, where the high concentration of carbonic species results in accelerated nucleation of zinc atoms with oxygen ions and carbon atoms from the dopant, which led to formation of larger particles [38]. Nonetheless, nanoparticle enhanced agglomeration in the presence of carbon resulted in the formation of highly mesoporous nanostructure which is the ideal electrode material for dye-sensitized solar cells (DSSC). We can conclude that an increase in carbon doping does affect the nanostructure morphology.

An elemental analysis of the unmodified ZnO and C-ZnO samples was performed with energy dispersive X-ray (EDX) spectroscopy, using a Scanning Electron Microscope (SEM). Inserts in Figure 4(b) show an elemental composition analysis of the ZnO samples. The EDX spectra of the ZnO samples and carbon modified samples reveal prominent EDX peaks at 0.51 keV, 1.01 keV, 1.49 keV, 8.87 keV, and 9.86 keV

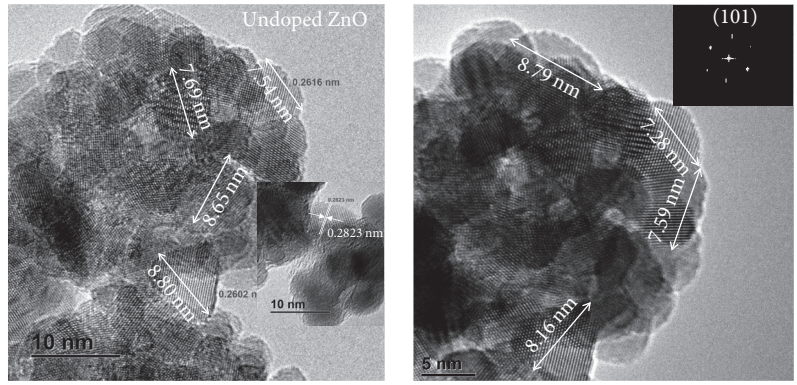

(a) (b)

Figure 5: HRTEM images of unmodified ZnO nanoparticles showing the same sample at different magnifications.

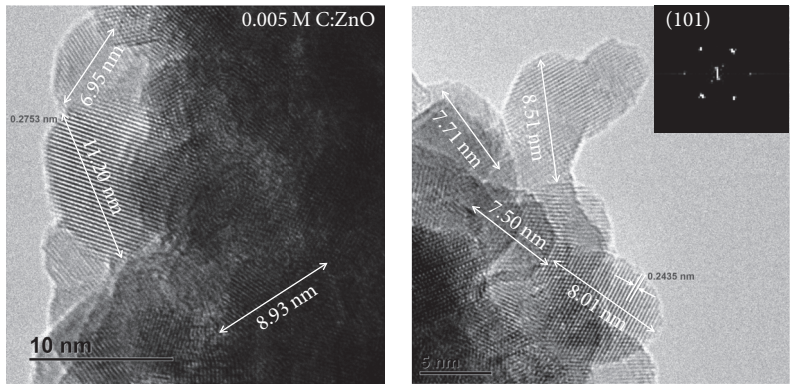

(a) (b)

Figure 6: HRTEM images of 0.05 M C-ZnO nanoparticles showing the same sample at different magnifications.

were observed. The X-ray energies of 0.51 keV and 1.01 keV represent the emissions from the K-shell of oxygen and L-shell of zinc, respectively. The X-ray energies at 8.87 keV and 9.86 keV are additional emissions from Zn core levels [34]. The presence of Zn, O, and C in the EDX spectra confirms the successful pyrolysis of zinc ethoxide to form ZnO nanostructures, as illustrated here by (1). Furthermore, the presence of C together with Zn and O atoms was shown by the EDX pattern of the C-modified samples, indicating the effective doping of the carbon in the ZnO matrix. Moreover, the EDX spectra of all the samples reveal the presence of Al in ZnO samples; this is due to the aluminium tube reactors and aluminium substrate holder employed in our pneumatic spray pyrolysis system.

3.3. HRTEM Analysis. A transmission electron microscope (TEM) was employed to determine the structural properties of ZnO nanoparticles synthesized by PSP technique. High resolution transmission electron microscopy images of the ZnO samples are shown here in Figures 5, 6, 7, and 8. HRTEM images have revealed that the synthesized nanoparticles are spherical, clustered, are agglomerated, which is in mutual agreement with SEM observations. In addition, the HRTEM analysis has revealed that the unmodified ZnO, 0.005 M C-ZnO, 0.01 M C-ZnO, and 0.015 M C-ZnO have spherical modal particle size diameters of about 8.80 nm, 8.93 nm, 10.46 nm, and 11.82 nm, respectively, which is in close agreement with those calculated from Scherer equation from XRD analysis in Table 2.

Furthermore, Figure 5(a) shows the highly crystalline structure of the unmodified ZnO nanoparticles with the spacing between the adjacent lattice planes of 0.26 nm and 0.28 nm corresponding to the distance between two (002) and (001) crystal planes of ZnO, respectively. The lattice spacing of 0.2602 is in mutual agreement with the ***d***-spacing of (002) planes of hexagonal Wurtzite ZnO structure [39]. Moreover, the HRTEM analysis is in mutual agreement with the XRD analysis. The corresponding selected area diffraction pattern (Figure 5(b)) (insert) obtained from the same spot of measurement also verifies the presence of (002) and (001) crystal planes of ZnO.

Figure 6 shows the HRTEM images of 0.005 C-ZnO samples synthesized by PSP technique. The HRTEM image analysis has revealed lattice spacings of 0.2753 nm and 0.2435 nm, corresponding to lattice plane of (100) and (101) of hexagonal Wurtzite ZnO structure [10, 39]. The lattice

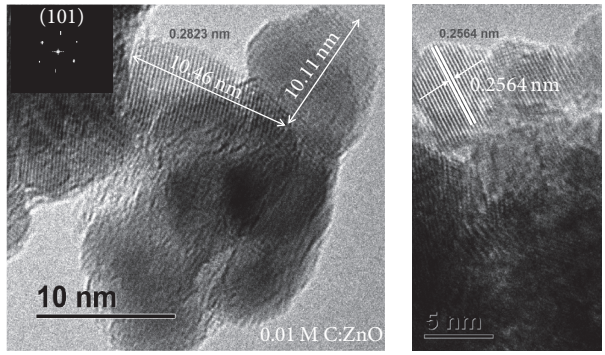

(a) (b)

Figure 7: HRTEM images of 0.01 M C-ZnO nanoparticles showing the same sample at different magnifications.

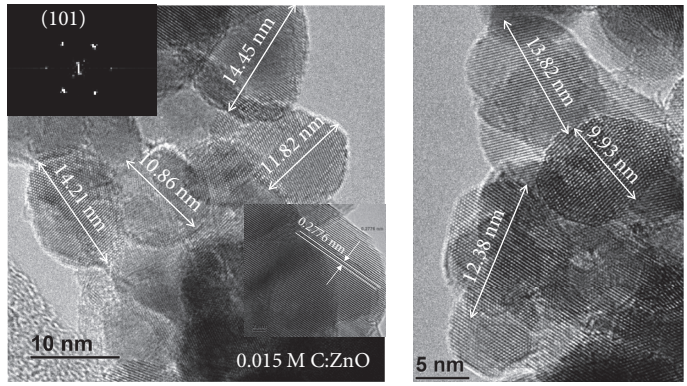

(a) (b)

Figure 8: HRTEM images of 0.015 M C-ZnO nanoparticles showing the same sample at different magnifications.

spacing of 0.2753 is somewhat greater than that of pure ZnO (0.26 nm). The HRTEM analysis is again consistent with the XRD analysis, which further confirms the substitutional replacement of the oxygen atom with the carbon atom in lattice structure of hexagonal Wurtzite ZnO. Moreover, the selected area diffraction image in Figure 6(b) has confirmed the presence of (101) planes of ZnO in the 0.005 M C-ZnO samples.

The lattice spacings for the 0.01 M C-ZnO and 0.015 M C-ZnO nanoparticles are shown here in Figure 7 and Figure 8. The HRTEM analysis has revealed a lattice spacing of 0.28 nm and 0.25 nm, which corresponds to lattice plane of (100) and (101) of hexagonal Wurtzite ZnO structure for the 0.01 M C-ZnO sample. In addition, the HRTEM analysis has revealed lattices spacing of 0.2776, which is close to the lattice spacing of 0.28 nm of (100) lattice plane of ZnO. In fact, all lattice parameters of the PSP synthesized samples remained the same, as all interplanar spacings measured through HR-TEM images tally to the planes of Wurtzite ZnO NPs, which is in agreement with XRD results.

Furthermore, all the selected electron diffraction (SAED) of the 0.01 M C-ZnO and 0.015 M C-ZnO nanoparticles, shown here in insert in Figure 8(a), has revealed a consisted pattern, similar to that of the unmodified sample in Figure 5(b) which further confirms that the carbon modified ZnO samples have a Wurtzite ZnO crystalline structure. This is in mutual agreement with the XRD analysis and the lattice spacings of the four samples do no differ that much.

Moreover, the increase in carbon doping from the estimated particle size is also consistent with XRD measurements and we also observed an increase in modal particle size as the concentration of carbon increases, and this again confirms the successful incorporation of C in ZnO, using the PSP technique which is in agreement with XRD observations.

3.4. Raman Spectroscopy Analysis. Raman spectroscopy is a technique where the sample under investigation is radiated with a laser, which excites electrons into higher energy states. Some of these energy states are called virtual states, where the electrons spend a rather short time before they relax back. The most probable relaxation pathway for the excited electrons is back to the same energy state from which they were excited [40]. This signal is denoted by Rayleigh scattering and is blocked by filters. What is measured instead is the energy of the light emitted when electrons relax back to a different vibration level, which gives information of the vibrational spectra of the sample [34, 40]. The spectrum obtained from a Raman measurement can be used in a number of ways, where the simplest one is to use it as a fingerprint for identification of species and crystal phases.

Table 3: Theoretical Raman vibrational frequencies and symmetry for bulk ZnO NPs obtained from a number of literature sources [12, 15, 37].

Frequency (cm^{-1})	102	330	379	437	541	577	592	660	1153
Symmetry	$E_2^{(1)}$(low)	Multiphonon	AO_1(TO)	$E_2^{(2)}$(high)	A_1(TA)	A_1(LO)	E_1(LO)	Multiphonon	Multiphonon

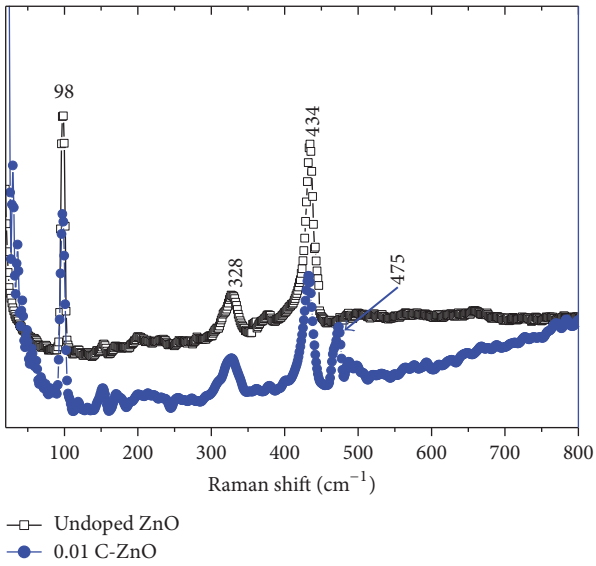

Figure 9: Raman spectra of unmodified ZnO and 0.01 M C-ZnO NPs synthesized by PSP technique.

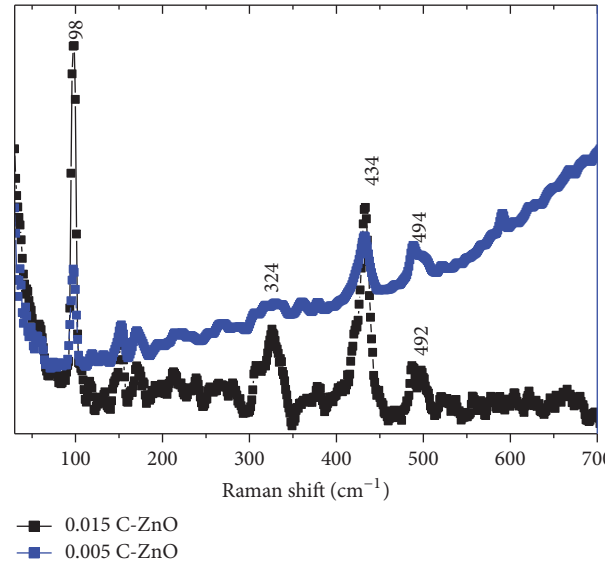

Figure 10: Raman spectra of 0.015 C-ZnO and 0.005 M C-ZnO NPs synthesized by PSP technique.

ZnO has a Wurtzite crystal structure, which belongs to the space group C_{6v}^4 with two formula units per primitive cell where all atoms occupy C_{3v}. The zone centre optical phonons predicted by group theory are classified as

$$\Gamma_{opt} = A_1 + 2B_1 + E_1 + 2E_2, \quad (3)$$

where A_1 and E_1 modes are polar and are split into the transverse optical Γ_{opt} and longitudinal optical LO phonons. In addition, E_2 mode consists of two modes: $E_2^{(2)}$(high) is associated with the vibration of oxygen atoms and $E_2^{(1)}$(low) is associated with the Zn sublattice [35, 40, 41]. Table 3 for comparison here presents the most typical frequencies and assignation of ZnO Raman active modes at room temperature.

Figures 9 and 10 present the Raman spectra from unmodified ZnO and C:ZnO NPs synthesized by PSP technique obtained under a 532 nm nonresonant green laser excitation source. For all RS spectra for the PSP synthesized samples in comparison with the Raman vibrational frequencies of bulk ZnO presented in Table 3, we can conclude that the prominent peak at 434 cm^{-1} observed is the distinctive peak of the Raman active principal $E_2^{(2)}$(high) mode of Wurtzite ZnO NPs [34, 35, 40, 41]. $E_2^{(2)}$(high) has been red shifted by 4 cm^{-1}, as compared to that found in bulk ZnO sample; this can be attributed to either (1) phonon confinement within the nanocrystal (quantum dots) boundaries or (2) the localization of phonons due to defects since nanoparticles or quantum dots (QDs) deposited by spray pyrolysis techniques inherently have more defects as compared to bulk crystals. Since the ZnO NPs fabricated by PSP technique have a particle size of ~9 nm, we would like to postulate that the red shift observed with PSP fabricated NPs might be due to both phonon confinement defects and tensile stress [40–42].

In comparison with Table 3, the less intense red shifted peak at 328 cm^{-1} for the 0.01 M and 0.015 M C:ZnO and 324 cm^{-1} for the unmodified ZnO and 0.005 M C:ZnO is assigned to $E_{2H} - E_{2L}$ multiphonon which is attributed to second-order Raman processes which redshift further with an increase in carbon doping concentration. The red shifted peak at 99 cm^{-1} is assigned to $E_2^{(1)}$(low), which is associated with Zn sublattice. We have also compared all the RS for the unmodified ZnO and C:ZnO samples to investigate how the carbon doping influences the Raman scattering of the ZnO NPs and whether new local vibration modes (LVM) exist in Raman spectra of C:ZnO NPs. Comparing the RS of the pure unmodified ZnO NPs and the C:ZnO NPs reveals new local vibration modes at 492 cm^{-1} for 0.005 M C:ZnO, 494 cm^{-1} for 0.015, and 475 cm^{-1} for 0.01 C:ZnO NPs in the Raman spectra. The LVMs of ZnO films modified with iron (Fe), antimony (Sb), aluminium (Al), gallium (Ga), and nitrogen (N) have been reported [43–45]. These LVMs are considered to be induced by certain doping agents. The presence of these LVMs can be used as an indication of dopant incorporation in the ZnO matrix, such as the LVM at 720 cm^{-1} for Fe modified, at 531 cm^{-1} for Sb modified, 631 cm^{-1} for Ga modified, and 411 cm^{-1} for Ag modified ZnO NPs. The existence of LVM modes has been attributed to impurity centres that break translational symmetry of the

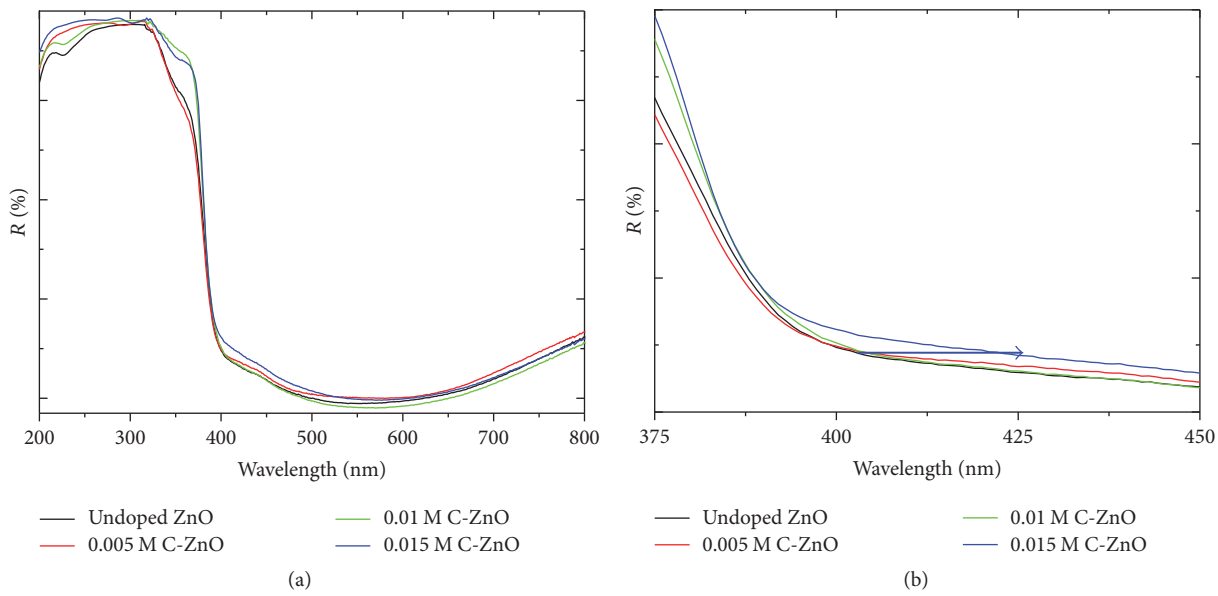

Figure 11: (a) The DRS spectra of the unmodified and C-ZnO samples synthesized by PSP technique and (b) the extended DRS spectra 375–450 nm.

crystal, in so doing, relaxing the conservation of the wave vector that results in the scattering of phonons in the host materials that have wave vectors far away from the zone centre [40, 45] indicating that, in our case, the new LVM observed in Raman spectra is due to the incorporation of carbon in our ZnO sample.

This analysis is in sync with our EDX and XRD analysis that confirmed the presence of carbon in PSP synthesized ZnO NPs. Moreover, this is also in close agreement with HRTEM analysis, which revealed an increase in **d**-spacing with the increase due to substitutional carbon doping. These observations also concur with the XRD analysis that revealed a peak shift of three dominant peaks with the increase in carbon concentration in our PSP synthesized samples.

3.5. UV-Vis Spectroscopy. It has been reported that the UV-Vis photosensitivity of wide band gap semiconductors is related to its band gap energy [36]. The UV-Vis diffuse reflectance spectra (DRS) of the PSP deposited C-ZnO samples are presented here in Figure 11 and, for the sake of comparison, the spectra of the unmodified ZnO sample are also presented here. UV-Vis DRS analysis has revealed that there is a shift in absorption edge with the increase in carbon dopant level. Figure 11(b) has revealed an increase in absorption properties with the increase in the concertation of carbon dopant.

The change in absorption properties is due to the fact that the unmodified ZnO samples, as calculated from XRD and HRTEM, have a smaller particle size, which revealed a general increase in NPs sizes with an increase in carbon dopant concertation. This confirms that the introduction of carbon into ZnO lattice introduced defects state of C above the valence band (VB) or below the conduction band (CB) [8, 35]. Moreover, it has been reported that the introduction of N into ZnO lattice, that is, N:ZnO, (N substituting O) pairs was liable to the existence of shallow acceptors that lie near the VB edge. Similarly, in this work, substitution of C also introduces similar phenomena [34, 45].

To quantitatively measure the type of band gap transition of the ZnO samples, the DRS data were fitted to equations for both direct and indirect band gap transitions. The profiles showed a perfect fit for direct band gap transition. The energy band gaps of the ZnO NPs were estimated by using

$$E_g = \frac{1239}{\lambda_{\text{Edge}}}\ \text{eV}. \tag{4}$$

The analysis has revealed that unmodified ZnO with modal nanoparticle size of 9.9 nm have an absorption edge at 374 nm and energy band gap of 3.31 eV which is larger than for bulk ZnO nanoparticle with an absorption edge at 388 nm and an energy band gap of 3.2 eV. The blue shift in the energy band gap of PSP of our synthesized samples, as compared to bulk ZnO, as previously reported, is due to the size confinement effect [31, 36]. However, the absorption edges for the 0.005 M, 0.01 M, and 0.015 M C-ZnO revealed a red shift with band gap energies of 3.29 eV, 3.28 eV, and 3.26 eV, respectively. The red shift in absorption properties for the PSP synthesized sample in this work has been attributed to increase in particle size (as evident from XRD and HRTEM analysis). This is also due to the substitutional carbon doping as is evident from HRTEM analysis which revealed increase in lattice parameters with increase in carbon doping and XRD analysis, which revealed a peak shift of the dominant peak to higher 2θ values with an increase in carbon doping. However, we would like to point out that, for these samples to be effective materials for solar cell electrodes, there is a need to increase the nanoparticle size to above 25 nm. This can be accomplished by increasing the concertation of the precursor of the starting solution to above 0.1 M.

4. Conclusions

In this study, C-modified ZnO NPs have been synthesized, using a pneumatic spray pyrolysis technique. The SEM images of both unmodified and C-ZnO samples reveal the formation of spherical shaped ZnO NPs. The SEM micrographs reveal that the morphology and shape of both unmodified and C-ZnO change as the dopant level increases. Moreover, the SEM-EDX analysis has confirmed the presence of Zn, C, and O in our samples, which confirms the successful pyrolysis of our precursor samples to ZnO nanostructures. XRD patterns of both unmodified and carbon modified ZnO samples have revealed characteristic hexagonal peaks of Wurtzite ZnO structure. XRD lines were observed at 31.90°, 34.50°, 36.34°, 47.73°, 56.88°, 63.04°, 68.20°, and 77.33°. These lines are indexed, respectively, as (100), (002), (101), (102), (110), (103), (200), and (112). The XRD and HRTEM analyses have revealed an increase in the nanoparticle size with an increase in C concentration. Additionally, the XRD analysis has revealed a peak shift to higher 20 values, which is indicative of substitutional carbon doping. The RS spectra of the PSP synthesized ZnO samples have shown a prominent peak at 434 cm^{-1} observed, that is, characteristic peak of the Raman active dominant $E_2^{(2)}$(high) mode of Wurtzite ZnO. The RS analysis has revealed new local vibration modes (LVM) at 492 cm^{-1} for 0.005 M C:ZnO, 494 cm^{-1} for 0.015, and 475 cm^{-1} for 0.01 C:ZnO, which may be used as a clear indication of the presence of C incorporated in ZnO lattice. UV-Vis DRS analysis has revealed a red shift with an increase in carbon doping.

Conflicts of Interest

The authors declare that they have no conflicts of interest.

Acknowledgments

The authors are grateful to the financial support from their sponsors, the South African National Research Foundation (NRF), the Govan Mbeki Research and Development Centre (GMRDC) of the University of Fort Hare, and the Sasol Inzalo Foundation. The authors would also like to acknowledge the DST/CSIR Nanotechnology Innovation Centre, National Centre for Nanostructured Materials, CSIR, and Centre of Image analysis and the University of Cape Town for the characterization of the ZnO NPs.

References

[1] X. Zhang, J. Qin, R. Hao et al., "Carbon-doped ZnO nanostructures: facile synthesis and visible light photocatalytic applications," *Journal of Physical Chemistry C*, vol. 119, no. 35, pp. 20544–20554, 2015.

[2] H. Ghaffarian, M. Saiedi, and M. A. Sayyadnejad, "Synthesis of ZnO nanoparticles by spray pyrolysis method," *Iran. J. Chem. Chem. Eng*, vol. 30, no. 1, p. 1, 2011.

[3] S. Dai, Y. Li, Z. Du, and K. R. Carter, "Electrochemical deposition of ZnO hierarchical nanostructures from hydrogel coated electrodes," *Journal of the Electrochemical Society*, vol. 160, no. 4, pp. D156–D162, 2013.

[4] S. P. Shrestha, R. Ghimire, J. J. Nakarmi et al., "Properties of ZnO:Al films prepared by spin coating of aged precursor solution," *Bulletin of the Korean Chemical Society*, vol. 31, no. 1, pp. 112–115, 2010.

[5] C.-Y. Tsay and K.-S. Fan, "Optimization of Zr-doped ZnO thin films prepared by sol-gel method," *Materials Transactions*, vol. 49, no. 8, pp. 1900–1904, 2008.

[6] L. An, J. Wang, T. Zhang, H. Yang, and Z. Sun, "Synthesis of ZnO nanoparticles by direct precipitation method," *Advanced Materials Research*, vol. 380, pp. 335–338, 2012.

[7] S. Hori, T. Suzuki, T. Suzuki, S. Miura, and S. Nonomura, "Effects of deposition temperature on the electrochemical deposition of zinc oxide thin films from a chloride solution," *Materials Transactions*, vol. 55, no. 4, pp. 728–734, 2014.

[8] D. E. Zhang, M. Y. Wang, J. J. Ma et al., "Enhanced photocatalytic ability from carbon-doped ZnO photocatalyst synthesized without an external carbon precursor," *Functional Materials Letters*, vol. 7, no. 3, Article ID 1450026, 2014.

[9] C.-C. Yu, W.-H. Lan, and K.-F. Huang, "Indium-nitrogen codoped zinc oxide thin film deposited by ultrasonic spray pyrolysis on n-(111) Si substrate: the effect of film thickness," *Journal of Nanomaterials*, vol. 2014, Article ID 861234, 2014.

[10] A. Bagabas, A. Alshammari, M. F. A. Aboud, and H. Kosslick, "Room-temperature synthesis of zinc oxide nanoparticles in different media and their application in cyanide photodegradation," *Nanoscale Research Letters*, vol. 8, no. 1, pp. 1–10, 2013.

[11] M. Ghosh, D. Karmakar, S. Basu et al., "Effect of size and aspect ratio on structural parameters and evidence of shape transition in zinc oxide nanostructures," *Journal of Physics and Chemistry of Solids*, vol. 75, no. 4, pp. 543–549, 2014.

[12] P. Kumar and Y. K. Walia, "Synthesis and structural properties of zinc oxide nano particles (ZnO NPs): a review," *Asian Journal of Advanced Basic Sciences*, vol. 2, no. 3, pp. 39–49, 2014.

[13] D. Li, M. Carette, A. Granier, J. P. Landesman, and A. Goullet, "Spectroscopic ellipsometry analysis of TiO_2 films deposited by plasma enhanced chemical vapor deposition in oxygen/titanium tetraisopropoxide plasma," *Thin Solid Films*, vol. 522, pp. 366–371, 2012.

[14] S. D. Lee, S. Nam, M. Kim, and J. Boo, "Synthesis and photocatalytic property of zno nanoparticles prepared by spray-pyrolysis method," *Physics Procedia*, vol. 32, pp. 320–326, 2012.

[15] H. Y. Yoo and S. Bruckenstein, "Synthesizing nanoparticles using reactions occurring in aerosol phases," *Advances in Nanoparticles*, vol. 02, no. 04, pp. 313–317, 2013.

[16] A. A. Oladiran and A. M. Olabis, "Synthesis and Characterization of ZnO nanoparticles with Zinc chloride as Zinc Source," *IOSR Journal of Applied Physics*, vol. 2, no. 2, 2013.

[17] S. Aydin, G. Turgut, M. Yilmaz, and M. Ertrugul, "Fabrication of ZnO nanorods by simplified spray pyrolysis," *Bitlis Eren University Journal of Science and Technology*, vol. 1, p. 1, 2011.

[18] T. Maekawa, K. Kurosaki, T. Tanaka, and S. Yamanaka, "Thermal conductivity of titanium dioxide films grown by metal-organic chemical vapor deposition," *Surface and Coatings Technology*, vol. 202, no. 13, pp. 3067–3071, 2008.

[19] E. Sarica and V. Bilgin, "Structural, optical, electrical and magnetic studies of ultrasonically sprayed ZnO thin films doped with vanadium," *Surface and Coatings Technology*, vol. 286, pp. 1–8, 2016.

[20] N. Sadananda Kumar, K. V. Bangera, and G. K. Shivakumar, "Effect of annealing on the properties of Bi doped ZnO thin films grown by spray pyrolysis technique," *Superlattices and Microstructures*, vol. 75, pp. 303–310, 2014.

[21] M. Nirmala and A. Anukaliani, "Synthesis and characterization of undoped and TM (Co, Mn) doped ZnO nanoparticles," *Materials Letters*, vol. 65, no. 17-18, pp. 2645–2648, 2011.

[22] S. Ozturk, N. Kilinic, N. Tsaltin, and Z. Z. Ozturk, "Fabrication of ZnO nanowires and nanorods," *Physica E: Low-Dimensional Systems and Nanostructures*, vol. 44, no. 6, pp. 1062–1065, 2012.

[23] C. F. Mah, K. P. Beh, F. K. Yam, and Z. Hassan, "Rapid formation and evolution of anodized-zn nanostructures in $NaHCO_3$ solution," *ECS Journal of Solid State Science and Technology*, vol. 5, no. 10, pp. M105–M112, 2016.

[24] R. Davinder, K. Mukesh, and K. A. Sandeep, "Deposition of nanocrystalline thin TiO_2 films for MOS capacitors using Sol-Gel spin method with Pt and Al top electrodes," *Solid-State Electronics*, vol. 76, pp. 71–76, 2012.

[25] A. Firoz and D. Viresh, "Tin sulfide (SnS) nanostructured films deposited by continuous spray pyrolysis (CoSP) technique for dye-sensitized solar cells applications," *Applied Surface Science*, vol. 358, pp. 491–497, 2015.

[26] E. Zaleta-Alejandre, J. Camargo-Martinez, A. Ramirez-Garibo et al., "Structural, electrical and optical properties of indium chloride doped ZnO films synthesized by Ultrasonic Spray Pyrolysis technique," *Thin Solid Films*, vol. 524, pp. 44–49, 2012.

[27] S. Barthwal, Y. S. Kim, and S.-H. Lim, "Fabrication of amphiphobic surface by using titanium anodization for large-area three-dimensional substrates," *Journal of Colloid and Interface Science*, vol. 400, pp. 123–129, 2013.

[28] M. Jyotia, D. Vijayb, and S. Radhac, "To Study the role of temperature and dodium hydroxide concentration in the synthesis of Zinc," *International Journal of Scientific and Research Publications*, vol. 3, no. 11, 2013.

[29] A. Bendavid, P. J. Martin, and E. W. Preston, "The effect of pulsed direct current substrate bias on the properties of titanium dioxide thin films deposited by filtered cathodic vacuum arc deposition," *Thin Solid Films*, vol. 517, no. 2, pp. 494–499, 2008.

[30] A. Anders, S. Lim, and K. M. Yu, "High quality ZnO:Al transparent conducting oxide films synthesized by pulsed filtered cathodic arc deposition," *Thin Solid Films*, vol. 518, no. 12, pp. 3313–3319, 2010.

[31] Z. Baji, Z. Lábadi, G. Molnár et al., "Highly conductive epitaxial ZnO layers deposited by atomic layer deposition," *Thin Solid Films*, vol. 562, pp. 485–489, 2014.

[32] R. Taziwa, E. L. Meyer, E. Sideras-Haddad, R. M. Erasmus, E. Manikandan, and B. W. Mwakikunga, "Effect of carbon modification on the electrical, structural, and optical properties of TiO_2 electrodes and their performance in labscale dye-sensitized Solar Cells," *International Journal of Photoenergy*, vol. 2012, Article ID 904323, 1 page, 2012.

[33] R. Taziwa and E. Meyer, "Carbon doped nano-crystalline TiO_2 photo-active thin film for solid state photochemical solar cells," *Advances in Nanoparticles*, vol. 3, no. 2, pp. 54–63, 2014.

[34] R. Kumari, A. Sahai, and N. Goswami, "Effect of nitrogen doping on structural and optical properties of ZnO nanoparticles," *Progress in Natural Science: Materials International*, vol. 25, no. 4, pp. 300–309, 2015.

[35] Y. Qiu, H. Fan, G. Tan, M. Yang, X. Yang, and S. Yang, "Effect of nitrogen doping on the photo-catalytic properties of nitrogen modified ZnO tetrapods," *Scientific reports*, vol. 5, 2014.

[36] S. M. Hosseini, I. A. Sarsari, P. Kameli, and H. Salamati, "Effect of Ag doping on structural, optical, and photocatalytic properties of ZnO nanoparticles," *Journal of Alloys and Compounds*, vol. 640, pp. 408–415, 2015.

[37] R. Wallace, A. P. Brown, R. Brydson, K. Wegner, and S. J. Milne, "Synthesis of ZnO nanoparticles by flame spray pyrolysis and characterisation protocol," *Journal of Materials Science*, vol. 48, no. 18, pp. 6393–6403, 2013.

[38] T. L. Tan, C. W. Lai, and S. B. Abd Hamid, "Tunable band gap energy of Mn-doped ZnO nanoparticles using the coprecipitation technique," *Journal of Nanomaterials*, vol. 2014, Article ID 371720, 2014.

[39] M. I. Khalil, M. M. Al-Qunaibit, A. M. Al-zahem, and J. P. Labis, "Synthesis and characterization of ZnO nanoparticles by thermal decomposition of a curcumin zinc complex," *Arabian Journal of Chemistry*, vol. 7, no. 6, pp. 1178–1184, 2014.

[40] I. Alessandro, S. Carvalho, R. L. Ribeiro et al., "Raman spectroscopy mapping of plasma thermally sprayed silicon sheet for solar cell substrate," *Journal of Materials Science and Engineering*, vol. 5, p. 561, 2011.

[41] A. A. Khan, A. F. Vladimir, M. Shamsa, and A. B. Alexander, "Micro-Raman investigation of optical phonons in ZnO nanocrystals," *Journal of Applied Physics*, vol. 97, no. 12, Article ID 124313, p. 124313, 2005.

[42] Y. Zhang, M. K. Ram, E. K. Stefanakos, and D. Y. Goswami, "Synthesis, characterization, and applications of ZnO nanowires," *Journal of Nanomaterials*, vol. 2012, Article ID 624520, 1 page, 2012.

[43] A. Escobedo-Morales and U. Pal, "Effect of In, Sb and Ga doping on the structure and vibrational modes of hydrothermally grown ZnO nanostructures," *Current Applied Physics*, vol. 11, no. 3, pp. 525–531, 2011.

[44] S.-S. Lo, D. Huang, C. H. Tu, C.-H. Hou, and C.-C. Chen, "Raman scattering and band-gap variations of Al-doped ZnO nanoparticles synthesized by a chemical colloid process," *Journal of Physics D: Applied Physics*, vol. 42, no. 9, Article ID 095420, 2009.

[45] M. Silambarasan, S. Saravanan, and T. Soga, "Raman and photoluminescence studies of Ag and Fe-doped ZnO nanoparticles," *International Journal of ChemTech Research*, vol. 7, no. 3, pp. 1644–1650, 2015.